4f spin driven ferroelectric-ferromagnetic multiferroicity in PrMn$_2$O$_5$ under a magnetic field

S. Chattopadhyay [1,*] V. Balédent,[2] S. K. Panda,[3] Sh. Yamamoto [1] F. Duc [4] T. Herrmannsdörfer,[1] M. Uhlarz,[1] T. Gottschall,[1] O. Mathon,[5] Z. Wang,[6] C. Strohm,[7] M. Greenblatt,[8] P. Foury-Leylekian,[2] and J. Wosnitza[1,9]

[1]*Dresden High Magnetic Field Laboratory (HLD-EMFL) and Würzburg-Dresden Cluster of Excellence ct.qmat, Helmholtz-Zentrum Dresden-Rossendorf, 01328 Dresden, Germany*

[2]*Université Paris-Saclay, CNRS, Laboratoire de Physique des Solides, 91405 Orsay, France*

[3]*Department of Physics, Bennett University, Greater Noida 201310, Uttar Pradesh, India*

[4]*Laboratoire National des Champs Magnétiques Intenses (LNCMI-EMFL), UPR 3228 CNRS, INSA, UGA, UPS, 143 avenue de Rangueil, 31400 Toulouse, France*

[5]*European Synchrotron Radiation Facility, Boîte Postale 220, 38043 Grenoble, France*

[6]*Anhui Province Key Laboratory of Condensed Matter Physics at Extreme Conditions, High Magnetic Field Laboratory of the Chinese Academy of Sciences, Hefei 230031, China*

[7]*Deutsches Elektronen-Synchrotron DESY, 22607 Hamburg, Germany*

[8]*Department of Chemistry and Chemical Biology, Rutgers, The State University of New Jersey, Piscataway, New Jersey 08854, USA*

[9]*Institut für Festkörper- und Materialphysik, Technische Universität Dresden, 01062 Dresden, Germany*

In contrast to all other members of the RMn$_2$O$_5$ family with nonzero 4f electrons (R = Nd to Lu), PrMn$_2$O$_5$ does not show any spin driven ferroelectricity in the magnetically ordered phase. By means of high-field electric polarization measurements up to 45 T, we have found that this exceptional candidate undergoes a spin driven multiferroic phase under magnetic field. X-ray magnetic circular dichroism studies up to 30 T at the Pr L_2 edge show that this ferroelectricity originates from and directly couples to the ferromagnetic component of the Pr^{3+} spins. Experimental observations along with our generalized gradient-approximation + U calculations reveal that this exotic ferroelectric-ferromagnetic combination stabilizes through the exchange-striction mechanism solely driven by a 3d-4f-type coupling, as opposed to the other RMn$_2$O$_5$ members with 3d-3d driven ferroelectric-antiferromagnetic-type conventional type-II multiferroicity.

I. INTRODUCTION

The research on functional materials, aiming at the next generation of smart devices, witnessed a massive upturn after the advent of materials showing multiple combined properties. Among such materials, an intriguing family of compounds known as magnetoelectric multiferroics (MEMF) with strongly coupled magnetism and ferroelectricity has attracted special attention [1–3]. For the MEMF family, reasons for being so highly sought after are twofold: (i) The microscopic origin of the magnetoelectric coupling is of fundamental interest that fascinates the condensed-matter community, and (ii) from an applied perspective, the spintronics and data-storage technologies would greatly benefit from such functionalities.

However, to be well suited for device applications, in addition to the room-temperature functionality, MEMF materials are expected to fulfill two very important criteria: The coexistence of ferromagnetism with ferroelectricity and strong coupling between the two order parameters. In reality, it is extremely difficult to satisfy both criteria simultaneously, and only a few single-phase materials are known to show coupling between the ferroelectric and ferromagnetic compo-

nents [4–6]. There are also a few theoretical works proposing strategies to couple ferroelectricity with weak ferromagnetism in a material [7,8].

Multiferroic materials have been classified into two types. In type-I materials, ferroelectricity and magnetism have different origins. However, in type-II multiferroics, spin driven ferroelectricity is caused by magnetic ordering itself, resulting in an intrinsically strong magnetoelectric coupling [3,9,10]. However, with the magnetism being frustrated in character, type-II multiferroics show the coexistence of complex antiferromagnetism and ferroelectricity. As multiferroics are relatively scarce, an important research activity focused on heterostructures with stacked ferromagnetic and ferroelectric layers [3]. However, as this eventually leads to type-I artificial multiferroics, the disadvantage of usually having small coupling remains unsolved.

In this context, studies on RMn$_2$O$_5$ (R = Bi, rare earth) oxides are particularly interesting. The RMn$_2$O$_5$ family is known for showing a series of magnetic transitions from R = Nd to Lu. The first magnetic transition around 40 ± 5 K to an incommensurate antiferromagnetic (AF) state is followed by a second transition, leading to a commensurate AF ordering of the Mn spins. An electric polarization P emerges with either the first (R = Tb, Sm, Nd) or the second magnetic transition along the b axis, asserting the type-II character of the

*s.chattopadhyay@hzdr.de

multiferroicity [11–20]. The associated strong coupling has been reported for $GdMn_2O_5$ and $TbMn_2O_5$, for which the electric polarization P can even be reversed by applying a modest magnetic field of a few teslas [1,2,21,22]. With lowering the temperature, a third magnetic transition generally appears, stabilizing another incommensurate AF order.

Neutron diffraction studies indicate that this spin-driven ferroelectricity is, in general, a consequence of a quasi-collinear ordering of the Mn spins (either the Mn^{3+} sublattice or both Mn^{3+} and Mn^{4+} sublattices) [11,12,14]. We note that, although the actual room-temperature crystal structure of RMn_2O_5 is already polar with a Pm (monoclinic) space group [23], the structural distortion with respect to the average nonpolar $Pbam$ space group [24,25] is so small that the induced polarization becomes extremely weak and cannot be measured directly in this regime. We will thus neglect this weak symmetry breaking in the following.

In RMn_2O_5, the long-standing debate on the microscopic origin of the spin driven ferroelectricity was resolved recently, confirming Mn-Mn exchange striction is the responsible one [12]. This result portrays the dominant role of the $3d$ ions and their frustrated superexchange interactions in the emergence of the spin driven ferroelectricity. Although known for a few other multiferroics [4,6,26], in RMn_2O_5, the role of the $4f$ ions was revealed only recently to explain the magnetoelectric behaviors in some candidates [27,28]. Particularly in $GdMn_2O_5$ and $NdMn_2O_5$, in addition to the dominant $3d$-$3d$ effect, a weak $3d$-$4f$ interaction was proposed to explain the observed spin driven ferroelectricity [15,29].

Among all compositions, $PrMn_2O_5$ appears to be an outstanding exception. In contrast to the other RMn_2O_5 members with nonzero numbers of $4f$ electrons, $PrMn_2O_5$ does not show any spin driven ferroelectricity. Powder neutron diffraction measurements show that Mn^{3+} moments order at $T_{N1} = 25$ K, following a magnetic propagation vector $q_1 = (0.5, 0, 0)$. With decreasing temperature, Mn^{4+} ordering appears at $T_{N2} = 18$ K with $q_2 = (0, 0, 0.5)$ [30]. Such distinct orderings of the Mn^{3+} and Mn^{4+} ions are indicative of a very weak exchange coupling between the two sublattices, explaining the absence of ferroelectricity. The Pr^{3+} sublattice does not fully order down to 1.5 K. Only a partial ordering of Pr^{3+} below T_{N1} was reported [30], suggesting a coupling between Mn^{3+} and Pr^{3+}. A powder neutron study under high pressure (a few GPa) shows the emergence of a collinear magnetic phase favorable for spin driven ferroelectricity [31]. However, electric polarization measurements were not possible to perform at this pressure regime to probe the possible onset of multiferroicity directly.

In this work, we report the emergence of a multiferroic phase under magnetic field in $PrMn_2O_5$. Using the combination of high-field electric polarization, x-ray magnetic circular dichroism (XMCD), and density functional theory (DFT)-based calculations, we show that unlike the multiferroicity observed in other RMn_2O_5 members, the spin driven ferroelectricity in $PrMn_2O_5$ originates from and couples to a ferromagnetic component. Moreover, the associated mechanism involved is no longer based on the $3d$-$3d$ coupling; rather, the spin driven ferroelectricity is solely a manifestation of the $3d$-$4f$ exchange interaction.

As mentioned, the presence of coupled ferroelectric and ferromagnetic components is very rare to find. In addition to that, $PrMn_2O_5$ hosts $3d$-$4f$ coupling and an exchange-striction mechanism. As separate phenomena, these features have been observed. However, a material like $PrMn_2O_5$, which hosts the simultaneous presence of all of these effects and mechanisms, is rather unique, to our knowledge.

Single crystals of $PrMn_2O_5$ from the same batch as mentioned in Ref. [23] were used for this study. The crystals were grown using the electrolysis method described in Refs. [32,33]. The as-grown crystals have a thin platelike morphology with the plate surface being perpendicular to the b axis.

II. RESULTS AND DISCUSSION

A. High-field electric polarization and magnetization

We carried out magnetic-field-dependent electric polarization P measurements up to 45 T using a pyroelectric technique at the Dresden High Magnetic Field Laboratory (HLD-EMFL). Field pulses of $\sim$20-ms duration were applied along b to measure the spin-induced pyroelectric current I along the same direction. A schematic diagram of the measurement technique is shown in the inset of the top panel of Fig. 1. Since the sweep rate of the magnetic field (dH/dt) is large in a pulsed field, dP/dt and hence the pyroelectric current become detectable even for a small change in P. The field-induced pyrocurrent I was recorded by measuring the voltage variation across a shunt resistor R_S. This shunt resistor was connected in series with the measurement circuit by a digital oscilloscope (Yokogawa DL750). The oscilloscope was operated with a high sampling rate of 1 MS s^{-1} and a resolution of 16 bits. The top panel of Fig. 1 shows the field dependence of I measured at 1.5, 7, and 22 K. The electric polarization was then calculated by integrating the $I(H)$ curves. The reproducibility of the data was verified carefully by repeating the measurements multiple times.

From the $P(H)$ data shown in the bottom panel of Fig. 1, it is evident that at 1.5 K, an electric polarization emerges above $\sim$12 T along the b direction. P increases with H and attains a maximum around 27 T. With a further increase in field, P decreases slowly and finally enters a flat region above 35 T. Notably, the polarization amplitude in $PrMn_2O_5$ ($\sim$1 nC/cm^2) is of the same order as that found in $NdMn_2O_5$, the adjacent member. The polarization gradually becomes weaker at higher temperatures and finally vanishes in the paramagnetic regime.

We also performed high-field magnetization measurements using pulsed magnetic fields at the HLD. Similar to the polarization measurements, the pulse duration was $\sim$20 ms. We repeated this measurement a few times to ensure the reproducibility of the data. Figure 2 shows $M(H)$ data measured at 1.5 K up to 42 T with H applied parallel to the b direction. In contrast to the polarization data, no anomaly is seen in $M(H)$ over the entire field range. The magnetization does not show any indication of saturation even at the highest field measured. In this system, the overall magnetization is dominated by the Mn moments. Therefore, the observed dissimilarities between the field dependence of the polarization and magnetization
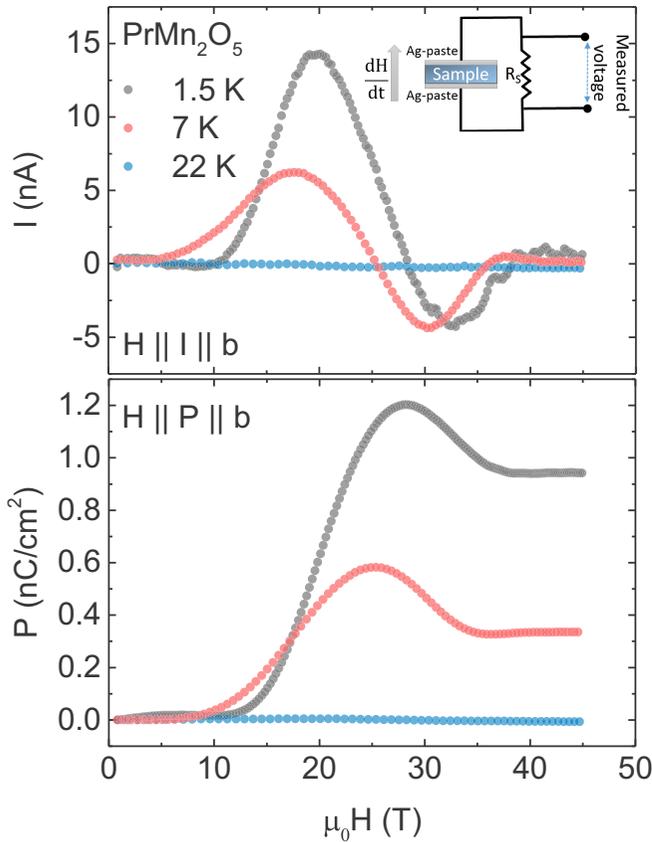
FIG. 1. The top panel shows the magnetic field H dependence of the pyrocurrent I up to 45 T at different temperatures using the $H \parallel I \parallel b$ configuration. The inset shows a schematic diagram of the pyroelectric technique used to record the field dependence of the pyrocurrent applying pulsed magnetic fields. The bottom panel depicts electric polarization P along the b axis as a function of magnetic field.

indicate that the magnetic field driven ferroelectricity does not seem to involve $3d$ ions directly. Rather, it indicates a possible $4f$ ion involvement in this case.
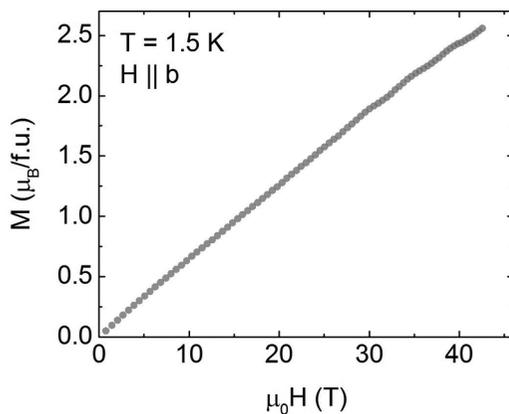
FIG. 2. Field dependence H of the magnetization M up to 42 T at 1.5 K with $H \parallel b$.
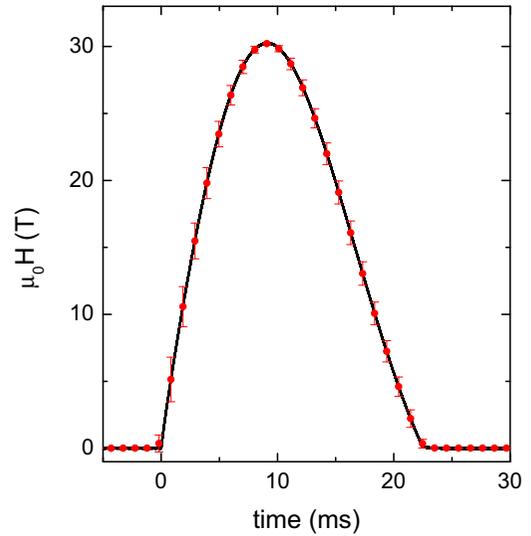
FIG. 3. Time profile of the magnetic field pulse used for the x-ray magnetic circular dichroism measurements.

B. High-field x-ray magnetic circular dichroism

In order to investigate the effect of a strong magnetic field on the rare-earth ordering, we performed XMCD measurements. The high-field XMCD measurements at the Pr L_2 edge were performed at energy dispersive x-ray absorption spectroscopy beamline ID24 at the European Synchrotron Radiation Facility (ESRF), Grenoble [34]. The pulsed-field magnet used for this purpose was connected to a 1.15-MJ portable power supply developed at the Laboratoire National des Champs Magnétiques Intenses, Toulouse. The magnet produces a maximum field of ~30 T with a rise time of ~10 ms and a total duration of ~23 ms (Fig. 3) every 8 min [35–37]. Figure 4(a) shows a representative x-ray absorption spectrum recorded at the Pr L_2 edge at 2 K. XMCD spectra were obtained in transmission mode at 2 K as the difference of x-ray absorption spectra when changing the field direction ($+b$ and $-b$ directions). The same measurement protocol was applied for both right- and left-handed circularly polarized x-ray beams. To record the field dependence of the absorption spectrum, a multiframe acquisition scheme with the high-frame-rate detector FReLoN (Fast-Readout Low Noise) was used, and a series of 50 full-energy spectra (i.e., acquisition windows of 1 ms) was recorded during each field pulse [38]. For our purpose, the crystal was mounted with the b axis parallel to the magnetic field and incident beam direction. The polished sample (thinned down to ~15 μm) was sandwiched between two diamond windows. This assembly was mounted in a dynamic He-flow cryostat in which the sample was cooled down through forced convection.

Figure 4(b) shows XMCD spectra recorded at magnetic fields between ~4.6 and ~30 T. The data presented here are a summation of 16 field pulses to improve the signal-to-noise ratio. The main contribution at the L_2 edge comes from the $2p_{1/2} \rightarrow 5d_{3/2}$ dipole transition according to the selection rules. As the magnetic field increases, the XMCD amplitude becomes more pronounced. The observed x-ray absorption spectra and dichroic spectra at the high-field regime are
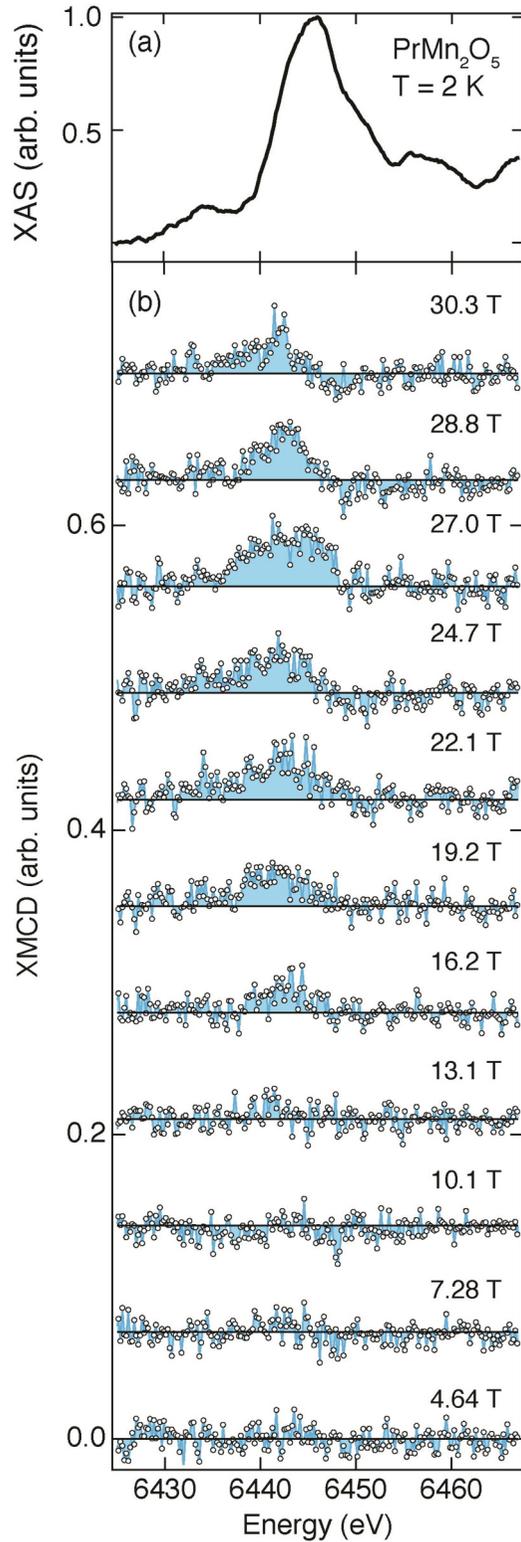
FIG. 4. (a) X-ray absorption spectrum (XAS) and (b) x-ray magnetic circular dichroism (XMCD) spectra at the Pr L_2 edge for $PrMn_2O_5$ with magnetic field applied parallel to the *b* axis at $T = 2$ K. Data sets for different magnetic fields are offset along the vertical axis for clarity.

consistent with those reported for other Pr^{3+}-based compounds ($4f^2$) [39,40].

The dichroic signal starts to appear at about 10 T, reaches its maximum around 27 T, and then drops gradually with a further increase in *H*. Although we cannot entirely exclude a contribution from the Mn ions, the Pr L_2 edge XMCD signal observed in $PrMn_2O_5$ is mainly caused by the Pr spins. The direct evidence can be seen from the peak shape of the XMCD signal. It does not change with field; only its amplitude gets modified, unlike garnet oxides [41,42], where the *L*-edge XMCD line shape and the amplitude change with field due to contributions of comparable strength from both $4f$ and $3d$ ions. In the case of intermetallic compounds composed of a $4f$ rare earth and a $3d$ transition metal, an earlier study reported a sizable transition-metal contribution as well to the rare-earth L_2 edge [43]. This is because the $3d$-$4f$ exchange interaction in such intermetallic compounds is mediated by the rare-earth $5d$ band which is directly accessed by the rare-earth *L* edge. Instead, in our system, the weaker superexchange $3d$-$4f$ interaction is mediated via the oxygen $2p$ state, which results in a marginal transition-metal contribution to the XMCD signals at the rare-earth *L* edges. Here, the mixed $4f$-$5d$ state of Pr^{3+} is the reason the transition toward $5d_{3/2}$ gives access to the $4f$ spin's ferromagnetic ordering. As a consequence, these results prove that the Pr ions contain a ferromagnetic component along the *b* axis under an external magnetic field applied along the same direction.

Notably, the field dependence of the integrated XMCD signal has a remarkable resemblance with the aforementioned polarization curve. In Fig. 5 we show the field dependence of both the integrated XMCD signal and polarization at comparable temperatures (2 K for XMCD and 1.5 K for *P*). The error bars shown are standard deviations extracted from the averaging procedure for 16 polarization-dependent spectra. The similarity between the quantities suggests that the two order parameters are coupled. The direct consequence is that $PrMn_2O_5$ becomes a type-II multiferroic under magnetic field with coupled ferromagnetism and ferroelectricity. Above
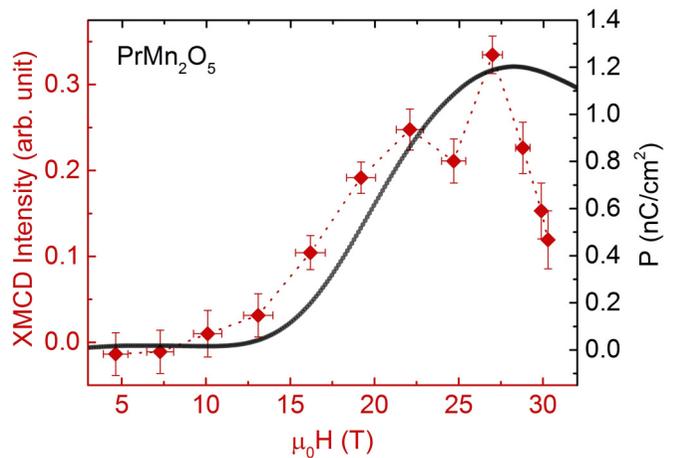
FIG. 5. Field dependence of the XMCD integrated intensity over the entire Pr L_2 edge range at 2 K compared with the field dependence of the electric polarization along the *b* axis at $T = 1.5$ K shown in Fig. 4. The dotted line is a guide to the eyes.

~27 T, the steeper decrease of the XMCD integrated intensity compared to the $P(H)$ behavior might come from the fact that the fluctuations of the signal at high magnetic field are larger, as reflected by the larger error bars when approaching 30 T. Therefore, the slope of the curve should be taken as an overall trend of the field dependence without considering it with high precision.

C. Density functional theory calculations

In order to provide further credence to our experimental findings, the DFT calculations were performed in the generalized gradient approximation + Hubbard U (GGA + U) approach by means of the full-potential linearized muffin-tin (MT) orbital method [44,45] as implemented in the RSPT code [46]. The Brillouin-zone (BZ) integration is carried out by using the thermal smearing method in a $8 \times 7 \times 10$ k mesh, which corresponds to 560 k points in the irreducible part of the BZ. For the charge density and potential angular decomposition inside the MT spheres, the value of maximum angular momentum was taken to be equal to $l_{max} = 8$. To describe the electron-electron correlation within the GGA + U approach, we used $U = 4$ eV and $J = 0.8$ eV for the Mn d states and $U = 5$ eV and $J = 0.5$ eV for the Pr f states.

The calculated projected densities of the states (PDOSs) are displayed in Fig. 6, which shows that the system is insulating with a gap of 1.2 eV. As expected, the Pr f states are highly localized. We observe that the majority-spin channel of Pr f states shows a valence band peak at around -1.3 eV binding energy and the rest of the states appear above the Fermi level between 3 and 5 eV, while the minority-spin channel is completely empty. Both the spin moment on the Pr site and the projected density of states are consistent with the nominal $4f^2$ state of the Pr ion. On the other hand, the occupied Mn d states are fairly delocalized within the binding energy range from -7 eV to the Fermi level. For both Mn^{4+} and Mn^{3+} ions, the majority channel is partially filled, while the minority channel is completely empty. The PDOS and the
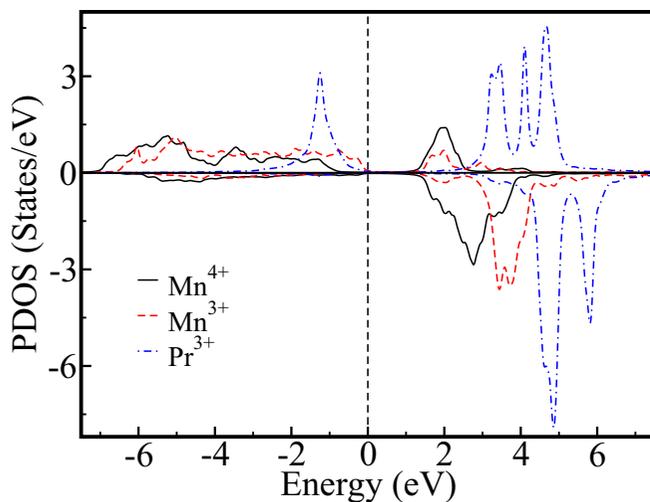
FIG. 6. Theoretically calculated partial density of states for Pr f and Mn d in the magnetic ground state.

TABLE I. The Mn-Mn and Mn-Pr exchange interactions (in meV) obtained from the converged GGA + U calculations using the magnetic-force theorem [49]. The negative values imply antiferromagnetic interaction.

J_i	Ions involved	Distance (Å)	Magnitude (meV)
J_1	Mn^{4+}-Mn^{4+}	2.95	-0.110
J_2	Mn^{4+}-Mn^{4+}	2.74	0.182
J_3	Mn^{3+}-Mn^{4+}	3.39	-0.040
J_4	Mn^{3+}-Mn^{4+}	3.61	-0.004
J_5	Mn^{3+}-Mn^{3+}	3.61	-0.205
J_6	Pr^{3+}-Mn^{3+}	3.35	0.009

projected moments are consistent with the tetravalent ($3d^3$) and trivalent ($3d^4$) states of Mn^{4+} and Mn^{3+}, respectively.

The obtained spin and orbital angular momenta of the Pr^{3+} ions are $1.81\mu_B$ and $1.99\mu_B$, respectively, and they are in opposite directions. The spin moment on Pr^{3+} is large, as expected from the nominal charge state (f^2). However, the presence of a strong reverse orbital moment makes the net moment very small ($0.18\mu_B$). It provides the explanation for the observed low moments on the Pr site in neutron experiments ($\sim 0.5\mu_B/Pr^{3+}$) [30]. The moments of Mn^{3+} and Mn^{4+} are essentially spin moments with estimated values of $3.38\mu_B$ and $2.55\mu_B$, respectively.

Further, to establish a spin model to understand the field dependence of the electric polarization and its relation to the long-range magnetic ordering, we estimated the interatomic magnetic exchange interactions from the converged GGA + U calculations using the formalism of Ref. [47]. We used the magnetic-force theorem [48,49] to extract the effective intersite exchange parameters J_{ij}. In this method, we mapped the total converged energies of the magnetic system onto the following Heisenberg-type spin Hamiltonian:

$$\hat{H} = -\sum_{i \neq j} J_{ij} \vec{S}_i \cdot \vec{S}_j. \tag{1}$$

Here, the indices i and j span the positions of the intrinsically magnetic ions, i.e., Pr^{3+}, Mn^{3+}, and Mn^{4+}. The effective J_{ij} is extracted in a linear-response manner via a Green's function technique. A detailed discussion of the implementation of the magnetic force theorem in RSPT is provided in Ref. [50]. All the calculations are carried out using the structural parameters given in Ref. [30]. The magnetic structure determination from neutron diffraction data shows that the magnetic moments of Pr^{3+} are parallel to their nearest-neighbor Mn^{3+} spins and they make only a small angle with respect to the a axis. Therefore, in the first approximation, we can safely ignore the anisotropic terms in the spin Hamiltonian. That is precisely the reason that we have considered only the isotropic Heisenberg exchange term in our model spin Hamiltonian.

The estimated exchange interactions are listed in Table I. These results are fully compatible with the magnetic structure reported in [30]. The interactions J_3 to J_6, which play a significant role in the present context, are presented in Fig. 7 along with the zero-field magnetic structure. The strongest interaction is J_5, imposing a perfect antiparallel alignment of the Mn^{3+} spins (represented in blue), along the direction of
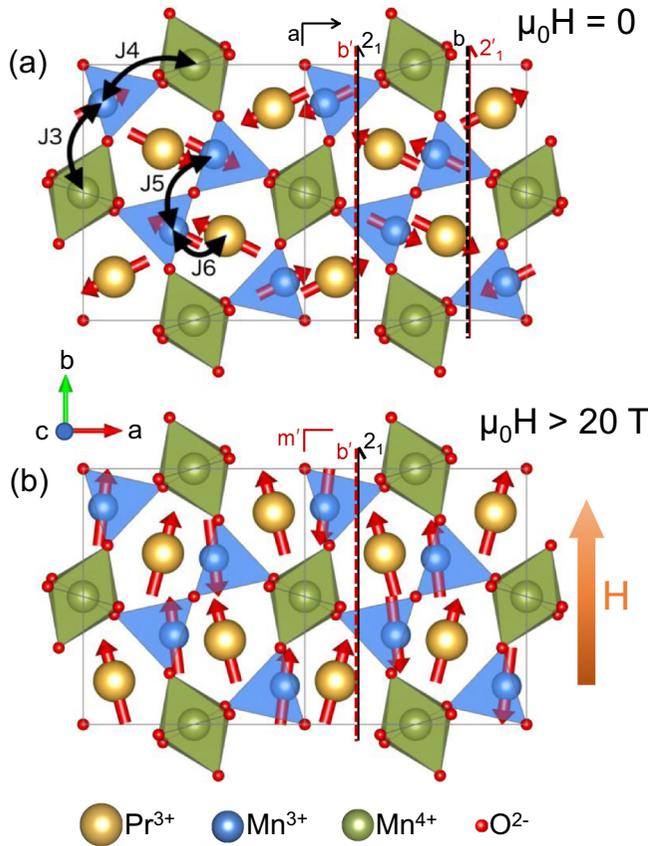
FIG. 7. (a) Schematic magnetic structure at zero field (magnetic space group $P_a b 2_1 a$) [30]. (b) Proposed schematic magnetic structure at high field in the ferroelectric phase (magnetic space group $Pb' 2_1 m'$). The amplitudes of the arrows showing the magnetic moments are not to the scale for the sake of clarity. Mn^{3+}, Mn^{4+}, and Pr^{3+} ions are represented in blue, green, and yellow, respectively.

anisotropy. The Pr moments (in yellow) are coupled to those Mn^{3+} only through a ferromagnetic J_6. Owing to the perfect colinearity of the Mn^{3+} and Pr^{3+} spins, it is reasonable to assume that the Pr anisotropy energy is negligible compared to J_6. Now, it is understandable why the Mn^{4+} (in green) moments are not coupled to the Mn^{3+} spins. Indeed, as can be seen in Table I, J_4 is almost two orders of magnitude smaller than J_5, excluding this path for connecting the two sublattices. The other possible connection between Mn^{3+} dimers goes via J_3, which is nearly an order of magnitude smaller than J_5. This interaction connects Mn^{4+} to two antiparallel Mn^{3+} spins. As a consequence, the two paths connecting Mn^{3+} and Mn^{4+} via J_3 exactly compensate each other. As for J_1 and J_2, they couple two Mn^{4+} moments along c. Symmetries of the magnetic structure are shown in Fig. 7(a), resulting in the magnetic space group $P_a b 2_1 a$. This space group is the same as the one reported for other members of the series, such as $GdMn_2O_5$ [15].

From the experimental results [30], we know that there are two distinct magnetic sublattices with separate ordering temperatures. The first one involves Mn^{3+} and Pr^{3+} spins, and the second one is formed by the Mn^{4+} spins. The fact that these two sublattices do not order at the same temperature

indicates that there is almost no coupling between the two. That is the reason why we considered only the Pr^{3+}-Mn^{3+} interaction J_6 and not the Pr^{3+}-Mn^{4+} one. As for the J_6 interaction, every Pr^{3+} ion is connected to two Mn^{3+} ions: One at 3.35-Å distance and another at 3.80-Å distance. Our calculations show that the Pr^{3+}-Mn^{3+} exchange corresponding to the distance of 3.80 Å is negligibly small due to the very large distance. In view of that, we have provided only the value of J_6 in Table I which actually corresponds to the Pr^{3+}-Mn^{3+} distance of 3.35 Å.

Interestingly, the Pr^{3+}-Mn^{3+} interaction J_6 is ferromagnetic as opposed to the antiferromagnetic Gd^{3+}-Mn^{3+} interaction in $GdMn_2O_5$ [15]. The primary reason for this could be attributed to the difference in the fillings of the f orbitals of these compounds. According to the extended Kugel-Khomskii model [51,52], the nature of the interatomic magnetic interaction primarily depends on three important parameters, namely, (i) crystal-field splitting, (ii) effective hopping strengths between the relevant orbitals participating in forming local magnetic moments, and (iii) the nominal fillings of those orbitals which determine whether the virtual hopping is allowed between them depending on their parallel or antiparallel alignment. The differences in the structural parameters of $GdMn_2O_5$ and $PrMn_2O_5$ will result in slight differences in the first two parameters. However, the most significant difference comes from the third point: The nominal occupancy of Pr^{3+} is f^2, while for Gd^{3+} it is f^7, which is exactly half filled. It is well established that half-filled orbitals promote antiferromagnetic superexchange since virtual hopping is allowed only if they possess antiparallel alignments, making AF ordering between Gd^{3+} and Mn^{3+} energetically favorable. However, for Pr^{3+}, f orbitals are less than half filled (f^2), and thus, virtual hopping between Pr^{3+} f and Mn^{3+} d is allowed for both parallel and antiparallel alignments, and the resulting exchange turns out to be ferromagnetic. A detailed calculation based on the Kugel-Khomskii model using calculated hopping and on-site energies is outside the scope of this work.

D. Origin of the field-induced ferroelectricity

On the basis of the estimated exchange interactions, we propose a possible model to couple the experimentally observed ferromagnetic component of Pr^{3+} to the induced ferroelectricity along the b direction. As mentioned, the essential components responsible for the magnetic order are J_5, connecting two Mn^{3+} spins, and J_6, connecting Mn^{3+} and Pr^{3+} spins. Upon increasing the external magnetic field along the b direction, both Mn^{3+} and Pr^{3+} spins are expected to align along b. Due to the strong J_5 interaction, Mn^{3+} will persist as an antiparallel dimer. This dimer will start rotating towards b as soon as the magnetic field exceeds the anisotropy energy of Mn. For the Pr^{3+} moments, there is a competition between two opposite interactions. On the one hand, the ferromagnetic interaction J_6 tries to align the Pr^{3+} spins parallel to the neighboring Mn^{3+} spins. As a consequence, Pr moments get antiferromagnetically aligned like the Mn^{3+} pairs. Then comes the Zeeman interaction term induced by the external magnetic field. It will push the Pr^{3+} spins to align along the b direction. As the XMCD results show, this happens above ~12 T, when

a ferromagnetic component of the Pr moments appears along b. A compatible magnetic structure preserving the maximum of the zero-field symmetries is schematically proposed in Fig. 7(b). The magnetic symmetry operations (represented on the magnetic structure) correspond to the magnetic space group $Pb'2_1m'$ ($Pm'c'2_1$, No. 26.70, in a conventional setting), a subgroup of P_ab2_1a. As a result, the two Mn^{3+}-Pr^{3+} pairs do not remain equivalent. A slight displacement of the oxygen ions bridging Mn^{3+} and Pr^{3+} is thus to be expected and would be different from one pair to the other. For the nearly ferromagnetically aligned Mn^{3+}-Pr^{3+} pair, this displacement will tend to maximize the nonfrustrated J_6 interaction. On the contrary, the oxygen displacement for the nearly antiferromagnetic Mn^{3+}-Pr^{3+} pair will tend to minimize this J_6 exchange coupling. Displacements are thus different from one side to the other, resulting in an effective polarization along b, as observed experimentally. From a structural point of view, the average centrosymmetric space group $Pbam$ at zero field is no longer compatible. The high-field space group is thus expected to be a noncentrosymmetric subgroup of $Pbam$ and compatible with the $Pm'c'2_1$ Shubnikov group. Among the two possible subgroups fulfilling the first constraint ($Pba2$ and $Pmc2_1$), only $Pmc2_1$ allows a polarization along the b direction. Fortunately, this group also satisfies the second requirement since it is a subgroup of $Pmc2_11'$. In conclusion, it is most likely that the high-field space group is $Pmc2_1$. This mechanism, leading to the coupling of a ferromagnetic Pr component and ferroelectricity, is thus mediated purely by a $3d$-$4f$ superexchange interaction. This is fundamentally different from the exchange-striction mechanism involved in the other members of the RMn$_2$O$_5$ family where a dominant $3d$-$3d$ interaction leads to the coupling between antiferromagnetism and ferroelectricity.

According to our DFT calculation and neutron diffraction results reported earlier [30], in $PrMn_2O_5$, the combined moment of Mn^{3+} and Mn^{4+} is much larger than that of Pr^{3+}. In the field-dependent magnetization shown in Fig. 2, only the b components of these moments contribute. The weak nature of the ferroelectricity and the measured XMCD signal signifies that the field-induced ferromagnetic component of Pr^{3+} spins along b, responsible for the breaking of centrosymmetry, leading to the emergence of ferroelectricity, is rather a small fraction of its already tiny total moment of about $0.18\mu_B$. That is why in the bulk magnetization measurement, where Pr^{3+}, Mn^{3+}, and Mn^{4+} contribute together, any possible characteristic contribution from Pr^{3+} spins in the vicinity of the field-induced polarization was not visible in the presence of a much larger background caused by the Mn moments. In contrast, an element-selective technique like XMCD was able to detect successfully even the small ferromagnetic component of Pr^{3+} along the b direction. In this context, it is also important to clarify that Fig. 7(b), which depicts our model to explain the field-induced ferroelectricity, is an exaggeration of the real scenario. To explain the symmetry-breaking mechanism with better clarity, we have chosen to show the emergence of the field-induced ferromagnetic component of the Pr^{3+} spins in an amplified way compared to what one expects in reality for the present situation. This is only for the sake of better visualization of the proposed model.

III. CONCLUSION

In conclusion, the combination of electric polarization and XMCD measurements in high magnetic fields along with DFT calculations reveals the emergence of spin-driven ferroelectricity in $PrMn_2O_5$ under magnetic field with strong magnetoelectric coupling. In contrast to other RMn$_2$O$_5$ members (R = Nd to Lu), multiferroicity in $PrMn_2O_5$ under magnetic field is characterized by coexisting ferroelectric and ferromagnetic components. The underlying mechanism for this spin-driven ferroelectricity involves an exchange-striction mechanism solely originating from $3d$-$4f$ coupling as opposed to the $3d$-$3d$-dominated multiferroicity in the other members. The observation of such a coupled ferroelectric-ferromagnetic state opens up new perspectives for technological applications. The present study evidences that there exists the possibility to stabilize a robust ferroelectric-ferromagnetic combination along with strong magnetoelectric coupling by manipulating the magnetic frustration using external parameters such as magnetic field and pressure.

[1] N. Hur, S. Park, P. A. Sharma, J. S. Ahn, S. Guha, and S.-W. Cheong, Nature (London) **429**, 392 (2004).

[2] S. W. Cheong and M. Mostovoy, Nat. Mater. **6**, 13 (2007).

[3] M. Fiebig, T. Lottermoser, D. Meier, and M. Trassin, Nat. Rev. Mater. **1**, 16046 (2016).

[4] Y. Tokunaga, S. Iguchi, T. Arima, and Y. Tokura, Phys. Rev. Lett. **101**, 097205 (2008).

[5] S. Ishiwata, Y. Taguchi, H. Murakawa, Y. Onose, and Y. Tokura, Science **319**, 1643 (2008).

[6] J. H. Lee, L. Fang, E. Vlahos, X. Ke, Y. W. Jung, L. F. Kourkoutis, J.-W. Kim, P. J. Ryan, T. Heeg, M. Roeckerath, V. Goian, M. Bernhagen, R. Uecker, P. C. Hammel, K. M. Rabe, S. Kamba, J. Schubert, J. W. Freeland, D. A. Muller, C. J. Fennie *et al.*, Nature (London) **466**, 954 (2010).

[7] C. J. Fennie, Phys. Rev. Lett. **100**, 167203 (2008).

[8] N. A. Benedek and C. J. Fennie, Phys. Rev. Lett. **106**, 107204 (2011).

[9] Y. Tokura, S. Seki, and N. Nagaosa, Rep. Prog. Phys. **77**, 076501 (2014).

[10] D. Khomskii, Physics **2**, 20 (2009).

[11] S. Chattopadhyay, V. Balédent, F. Damay, A. Gukasov, E. Moshopoulou, P. Auban-Senzier, C. Pasquier, G. André, F. Porcher, E. Elkaim, C. Doubrovsky, M. Greenblatt, and P. Foury-Leylekian, Phys. Rev. B **93**, 104406 (2016).

[12] G. Yahia, F. Damay, S. Chattopadhyay, V. Balédent, W. Peng, E. Elkaim, M. Whitaker, M. Greenblatt, M.-B. Lepetit, and P. Foury-Leylekian, Phys. Rev. B **95**, 184112 (2017).

[13] V. Polyakov, V. Plakhty, M. Bonnet, P. Burlet, L.-P. Regnault, S. Gavrilov, I. Zobkalo, and O. Smirnov, Phys. B (Amsterdam, Neth.) **297**, 208 (2001).

[14] G. R. Blake, L. C. Chapon, P. G. Radaelli, S. Park, N. Hur, S-W. Cheong, and J. Rodríguez-Carvajal, Phys. Rev. B **71**, 214402 (2005).

[15] G. Yahia, F. Damay, S. Chattopadhyay, V. Balédent, W. Peng, S. W. Kim, M. Greenblatt, M.-B. Lepetit, and P. Foury-Leylekian, Phys. Rev. B **97**, 085128 (2018).

[16] B Roessli, P. Fischer, P. J. Brown, M. Janoschek, D. Sheptyakov, S. N. Gvasaliya, B. Ouladdiaf, O. Zaharko, E. Golovenchits, and V. Sanina, J. Phys.: Condens. Matter **20**, 485216 (2008).

[17] M. Fukunaga, Y. Sakamoto, H. Kimura, Y. Noda, N. Abe, K. Taniguchi, T. Arima, S. Wakimoto, M. Takeda, K. Kakurai, and K. Kohn, Phys. Rev. Lett. **103**, 077204 (2009).

[18] Y. Noda, H. Kimura, M. Fukunaga, S. Kobayashi, I. Kagomiya, and K. Kohn, J. Phys.: Condens. Matter **20**, 434206 (2008).

[19] M. Fukunaga, Y. Sakamoto, H. Kimura, and Y. Noda, J. Phys. Soc. Jpn. **80**, 014705 (2011).

[20] I. Kagomiya and K. Kohn, Ferroelectrics **219**, 169 (1998).

[21] P. G. Radaelli and L. C. Chapon, J. Phys.: Condens. Matter **20**, 434213 (2008).

[22] N. Hur, S. Park, P. A. Sharma, S. Guha, and S.-W. Cheong, Phys. Rev. Lett. **93**, 107207 (2004).

[23] V. Balédent, S. Chattopadhyay, P. Fertey, M. B. Lepetit, M. Greenblatt, B. Wanklyn, F. O. Saouma, J. I. Jang, and P. Foury-Leylekian, Phys. Rev. Lett. **114**, 117601 (2015).

[24] I. Kagomiya, K. Kohn, and T. Uchiyama, Ferroelectrics **280**, 131 (2002).

[25] J. A. Alonso, M. T. Casais, M. J. Martinez-Lope, J. L. Martinez, and M. T. Fernandez-Diaz, J. Phys.: Condens. Matter **9**, 8515 (1997).

[26] B. Lorenz, Y. Q. Wang, Y. Y. Sun, and C. W. Chu, Phys. Rev. B **70**, 212412 (2004).

[27] S. Chattopadhyay, S. Petit, E. Ressouche, S. Raymond, V. Balédent, G. Yahia, W. Peng, J. Robert, M.-B. Lepetit, M. Greenblatt, and P. Foury-Leylekian, Sci. Rep. **7**, 14506 (2017).

[28] M. Deutsch, W. Peng, P. Foury-Leylekian, V. Balédent, S. Chattopadhyay, M. T. Fernandez-Diaz, T. C. Hansen, A. Forget, D. Colson, M. Greenblatt, M.-B. Lepetit, S. Petit, and I. Mirebeau, Phys. Rev. B **98**, 024408 (2018).

[29] S. Mansouri, S. Jandl, M. Balli, P. Fournier, B. Roberge, M. Orlita, I. A. Zobkalo, S. N. Barilo, and S. V. Shiryaev, Phys. Rev. B **98**, 205119 (2018).

[30] C. Doubrovsky, G. André, A. Gukasov, P. Auban-Senzier, C. R. Pasquier, E. Elkaim, M. Li, M. Greenblatt, F. Damay, and P. Foury-Leylekian, Phys. Rev. B **86**, 174417 (2012).

[31] W. Peng, V. Balédent, S. Chattopadhyay, M.-B. Lepetit, G. Yahia, C. V. Colin, M. J. Gooch, C. R. Pasquier, P. Auban-Senzier, M. Greenblatt, and P. Foury-Leylekian, Phys. Rev. B **96**, 054418 (2017).

[32] G. Popov, M. Greenblatt, and W. McCarroll, Mater. Res. Bull. **35**, 1661 (2000).

[33] B. Wanklyn, J. Mater. Sci. **7**, 813 (1972).

[34] S. Pascarelli, O. Mathon, T. Mairs, I. Kantor, G. Agostini, C. Strohm, S. Pasternak, F. Perrin, G. Berruyer, P. Chappelet, C. Clavel, and M. C. Dominguez, J. Synchrotron Radiat. **23**, 353 (2016).

[35] P. van der Linden, O. Mathon, C. Strohm, and M. Sikora, Rev. Sci. Instrum. **79**, 075104 (2008).

[36] P. Frings, J. Vanacken, C. Detlefs, F. Duc, J. E. Lorenzo, M. Nardone, J. Billette, A. Zitouni, W. Bras, and G. L. J. A. Rikken, Rev. Sci. Instrum. **77**, 063903 (2006).

[37] F. Duc, X. Fabrèges, T. Roth, C. Detlefs, P. Frings, M. Nardone, J. Billette, M. Lesourd, L. Zhang, A. Zitouni, P. Delescluse, J. Béard, J. P. Nicolin, and G. L. J. A. Rikken, Rev. Sci. Instrum. **85**, 053905 (2014).

[38] C. Strohm, F. Perrin, M.-C. Dominguez, J. Headspith, P. vander Linden, and O. Mathon, J. Synchrotron Radiat. **18**, 224 (2011).

[39] A. M. G. Carvalho, F. Garcia, V. S. R. de Sousa, P. J. von Ranke, D. L. Rocco, G. D. Loula, E. J. de Carvalho, A. A. Coelho, L. M. da Silva, and F. C. G. Gandra, J. Magn. Magn. Mater. **321**, 3014 (2009).

[40] Y. E. Samoshkina and A. Rogalev, J. Exp. Theor. Phys. **126**, 660 (2018).

[41] N. Kawamura, M. Suzuki, H. Maruyama, and T. Ishikawa, J. Synchrotron Radiat. **8**, 425 (2011).

[42] C. Strohm, P. van der Linden, O. Mathon, and S. Pascarelli, Phys. Rev. Lett. **122**, 127204 (2019).

[43] J. Chaboy, M. A. Laguna-Marco, C. Piquer, R. Boada, H. Maruyama, and N. Kawamura, J. Synchrotron Radiat. **15**, 440 (2008).

[44] O. K. Andersen, Phys. Rev. B **12**, 3060 (1975).

[45] J. M. Wills and B. R. Cooper, Phys. Rev. B **36**, 3809 (1987).

[46] J. M. Wills, O. Eriksson, M. Alouni, and D. L. Price, *Electronic Structure and Physical Properties of Solids: The Uses of the LMTO Method* (Springer, Berlin, 2000).

[47] Y. O. Kvashnin, O. Grånäs, I. Di Marco, M. I. Katsnelson, A. I. Lichtenstein, and O. Eriksson, Phys. Rev. B **91**, 125133 (2015).

[48] A. Liechtenstein, M. Katsnelson, V. Antropov, and V. Gubanov, J. Magn. Magn. Mater. **67**, 65 (1987).

[49] M. I. Katsnelson and A. I. Lichtenstein, Phys. Rev. B **61**, 8906 (2000).

[50] S. K. Panda, Y. O. Kvashnin, B. Sanyal, I. Dasgupta, and O. Eriksson, Phys. Rev. B **94**, 064427 (2016).

[51] K. I. Kugel and D. I. Khomskii, Zh. Eksp. Teor. Fiz. **64**, 1429 (1973).

[52] K. I. Kugel and D. I. Khomskii, Sov. Phys. Usp. **25**, 231 (1982).